ACS APPLIED MATERIALS & INTERFACES

Research Article

www.acsami.org

Mesoporous Gold and Palladium Nanoleaves from Liquid–Liquid Interface: Enhanced Catalytic Activity of the Palladium Analogue toward Hydrazine-Assisted Room-Temperature 4-Nitrophenol Reduction

Soumen Dutta, Sougata Sarkar, Chaiti Ray, Anindita Roy, Ramkrishna Sahoo, and Tarasankar Pal*

Department of Chemistry, Indian Institute of Technology, Kharagpur – 721302, India

Supporting Information

ABSTRACT: The importance of an interfacial reaction to obtain mesoporous leafy nanostructures of gold and palladium has been reported. A new synthetic strategy involving 1,4-dihydropyridine ester (DHPE) as a potential reducing agent performs exceptionally well for the desired morphologies of both the noble metals at room temperature. The DHPE in turn transforms into its oxidized aromatic form. The as-synthesized gold leaves exhibit high surface-enhanced Raman scattering activity with rhodamine 6G (R6G) due to their hyperbranched structure. It is worthwhile that as-synthesized porous architectures of palladium support the room-temperature hydrogenation of 4-nitrophenol (4-NP) by hydrazine hydrate ($N_2H_4{\cdot}H_2O$), reported for the first time. Furthermore, MPL exhibits exceptionally good catalytic activity toward electrooxidation of formic acid. Therefore, an aromaticity driven synthetic technique achieves a rationale to design leafy nanostructures of noble metals from the liquid–liquid interface for multifaceted applications.

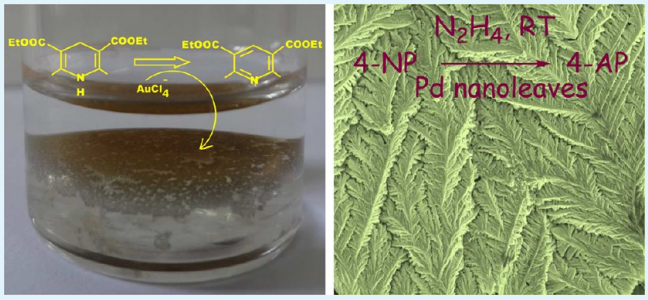

KEYWORDS: *interfacial reaction, leafy nanostructure, aromaticity driven, noble metals, hydrogenation, 4-nitrophenol*

INTRODUCTION

Noble metal nanoparticles have been attracting huge attention over the past decades due to their tunable physical and chemical properties with respect to their intriguing morphologies that support their potential applications in diverse fields, such as spectroscopy, catalysis, sensing, and so forth.[1] Among the various noble metal nanoparticles, gold nanoparticles have gained huge attention over the past few decades for their unique optical, catalytic, and electronic properties with exceptionally high chemical stability.[2,3] Gold nanoparticles with varied morphologies, such as rods,[4] wires,[5] prisms,[6] plates,[7] stars,[8] flowers,[9] rosettes,[10] cones,[11] cubes,[12] dendrites,[13] etc., were successfully synthesized by different groups. Three-dimensional dendritic superstructures are nowadays reported frequently and also become very interesting due to their reasonable growth mechanism as well as their various attractive properties.[13−18] Complex gold structures provide clean surfaces for ultrahigh Raman enhancement of a molecule from their inherited numerous "hot spots" at the faceted edges or corners of Au nanostructures.[13,17] Generally, galvanic exchange,[14] electrochemical,[15,16] surfactant-assisted,[17] or wet-chemical methods[18] were considered for the fabrication of branched structure of gold. Herein, a new synthetic technique has been adopted for the evolution of leafy superstructure of gold at the liquid–liquid interface. Previously, the air–water interface was used for various morphologies of gold,[19−21] but the liquid–liquid interfacial technique for gold nanostructures was studied in limited cases.[11,22] Moreover, 1,4-dihydropyridine ester (DHPE), an analogue of naturally reduced nicotinamide adenine dinucleotide phosphate (NADPH), has been successfully employed here just like its use in various organic transformations as a hydrogenating or reducing agent, which, in turn, transforms into its aromatic form.[23,24] Thus, the aromaticity driven reaction capability of this reagent for the synthesis of noble metal nanostructures becomes the first report of its kind. It is worthwhile that the present study involves DHPE in organic solvent and reduces aqueous gold chloride solution at room temperature, which results in a special three-dimensional leafy structure of gold with a mesoporous backbone at the liquid–liquid interface. The aromaticity driven redox reaction is prompted well under UV irradiation, generating a morphologically important product. Fabrication of mesoporous gold through a new synthetic approach is highly demanding due to its increased surface area, which controls their applications in various fields.[25−28]

Palladium nanoparticles are admirable for their excellent catalytic properties,[29] which results in tremendous efforts for the synthesis of various morphologies[30,31] or compositions[32] of

Received: February 25, 2014
Accepted: May 29, 2014
Published: May 29, 2014

Scheme 1. Synthetic Procedure for the Evolution of MGL and Their Microscopic Image

palladium nanoparticles with improved catalytic activity. In that context, a porous architecture with leafy or dendritic morphologies of Pd is thought to be a promising catalyst for facile reduction of 4-nitrophenol (4-NP), a benchmark substrate[33] in metal nanoparticle mediated catalysis at room temperature. Although very few reports are found on branched Pd nanostructures,[31,34,35] our proposed interfacial synthetic strategy performs exceptionally well to fabricate mesoporous Pd nanoleaves at room temperature.

EXPERIMENTAL SECTION

Materials. All the reagents used were of AR grade and used as received without further purification. Gold chloride ($HAuCl_4 \cdot 3H_2O$), palladium chloride ($PdCl_2$), paraformaldehyde, ethyl acetoacetate, ammonium acetate, and 2-ethoxyaniline were purchased from Aldrich. All the solvents such as dichloromethane (DCM), ethyl acetate (EtOAc), dimethyl sulfoxide (DMSO), acetonitrile (CH_3CN), chloroform ($CHCl_3$), and ethanol were bought from Merck, India. Hydrazine hydrate, all the nitroaromatic compounds, rhodamine 6G (R6G), sodium fluoride (NaF), sodium bromide (NaBr), sodium chloride (NaCl), sodium nitrate ($NaNO_3$), anhydrous magnesium sulfate, and cetyltrimethylammonium bromide (CTAB) were obtained from SRL, India. Formic acid (~99%) and H_2SO_4 were purchased from Merck, India. All glassware was cleaned using aqua-regia, subsequently rinsed with a copious amount of double-distilled water, and dried well prior to use. Double-distilled water was used throughout the course of the experiment.

Synthesis of Mesoporous Gold Leaves (MGL). 1,4-Dihydropyridine ester (DHPE) was prepared from paraformaldehyde, ethyl acetoacetate, and ammonium acetate as reported previously.[36] An interfacial synthetic mechanism was followed for mesoporous gold nanoleaves (MGL) synthesis. In short, 3 mg of DHPE was first dissolved in DCM (3 mL), and into this mixture an aqueous solution of gold chloride (3 mL; 1.67×10^{-3} M) was added. Then, the whole mixture was irradiated under UV light (15 W fluorescent lamp containing high-pressure Hg vapor; wavelength = 365 nm) for 12 h. Here, the UV light irradiates the sample mixture from the top at a distance of about 20 cm, and the corresponding schematic representation for the experimental setup is shown in Scheme S1 (Supporting Information). Completion of the reaction was indicated by the disappearance of the aqueous yellow-colored solution (i.e., gold chloride) in the upper layer. As-synthesized MGL were recovered carefully from the interface of two layers, and then they were washed repeatedly with ethyl acetate (EtOAc) to remove any organic molecules. The same procedure was also followed for other cases except for the accumulation of various salts (e.g., NaF, NaCl, NaBr, and $NaNO_3$) or stabilizers (CTAB) in aqueous medium at their respective concentration.

Synthesis of Mesoporous Palladium Leaves (MPL). Mesoporous palladium leaves (MPL) were synthesized in the same procedure as indicated above except for the precursor salts of palladium.

Instrumentation. FESEM analysis was done with a supra, Carl Zeiss Pvt. Ltd. Instrument, and compositional analysis of the sample was completed with an energy-dispersive X-ray microanalyzer (OXFORD ISI 300 EDAX) attached to the scanning electron microscope. Transmission electron microscopic (TEM) analyses of the samples were carried out on a Hitachi H-9000 NAR transmission electron microscope, operating at 100 kV. XRD was recorded on a Philips PW-1710 X-ray diffractometer (40 kV, 20 mA) with Cu Kα radiation (λ = 1.5418 Å) in the 2θ range of 30−80° at a scanning rate of 0.5° min^{-1}. X-ray photoelectron spectroscopy (XPS) analysis was performed with a VG Scientific ESCALAB MK II spectrometer (UK) equipped with a Mg Kα excitation source (1253.6 eV) and a five-channeltron detection system to analyze the elemental state. Nitrogen adsorption and desorption measurements were done at 77 K using a Quantachrome Autosorb Automated Gas Sorption System after the samples were degassed in a vacuum overnight, and Brunauer−Emmett−Teller (BET) and Barrett−Joyner−Halenda (BJH) calculations were performed for the analysis of surface area and pore-size distribution, respectively. Raman spectra were obtained with a Renishaw Raman Microscope, equipped with a He−Ne laser excitation source (wavelength = 632.8 nm), and a Peltier cooled (−70 °C) charge-coupled device (CCD) camera. A Leica microscope with a 50× objective lens was used. The holographic grating with 1800 grooves/mm and the 1 cm^{-1} slit enabled the spectral resolution. The laser power at the sample was 4.5 mW, and the data acquisition time was 30 s. The ^{1}H NMR spectrum was obtained with a Bruker DPX-200 MHz NMR instrument. Atomic force microscopic (AFM) analysis was performed by an Agilent Technologies SPM 5500 instrument. UV−vis spectra were recorded in a Spectrascan UV 2600 spectrophotometer (Chemito, India). Cyclic voltammetry (CV) measurements were conducted in a CHI660E electrochemical workstation with a three-electrode system with a Pt counter electrode, Ag/AgCl as reference electrode, and a catalyst modified glassy carbon electrode (GCE) as the working electrode.

Preparation of Samples for Surface-Enhanced Raman Scattering (SERS). For SERS measurement, rhodamine 6G (R6G) solutions were prepared with variable concentrations in ethanol with proper dilution. To each 1 mL of R6G solution, 50 μL of MGL (1 mg/mL in ethanol) was added and left for 2 h incubation. Then, the samples were washed properly with ethanol and spotted on aluminum foil for SERS experiment.

Reduction of Nitroaromatics by Mesoporous Palladium Leaves (MPL). The catalytic reduction of nitroaromatics was performed in a well-stoppered cuvette in an ambient condition. Nitroaromatic compounds (30 μL; 10^{-2} M) and hydrazine hydrate (0.3 mL; 0.1 M) were first diluted to a 3 mL aqueous solution where the concentration became 10^{-4} and 10^{-2} M, respectively. Then, 0.25 mg of catalyst, i.e., MPL, was added from outside, and the reduction process was followed through spectrophotometrically by recording the absorbance value in the UV−vis spectra. Here, 4-nitrophenol (4-NP), 2-nitroaniline (2-NA), and 4-nitroaniline (4-NA) were taken for reduction by hydrazine in the presence of MPL. The effect of catalyst dose on 4-NP reduction was studied by varying its amount.

RESULTS AND DISCUSSION

Scheme 1 represents the synthetic approach for the evolution of mesoporous gold with leafy nanostructures (MGL) at the liquid−liquid ("dichloromethane−water") interface. The chemistry involves the spontaneous reduction of an aqueous solution

dx.doi.org/10.1021/am503251r | ACS Appl. Mater. Interfaces 2014, 6, 9134−9143

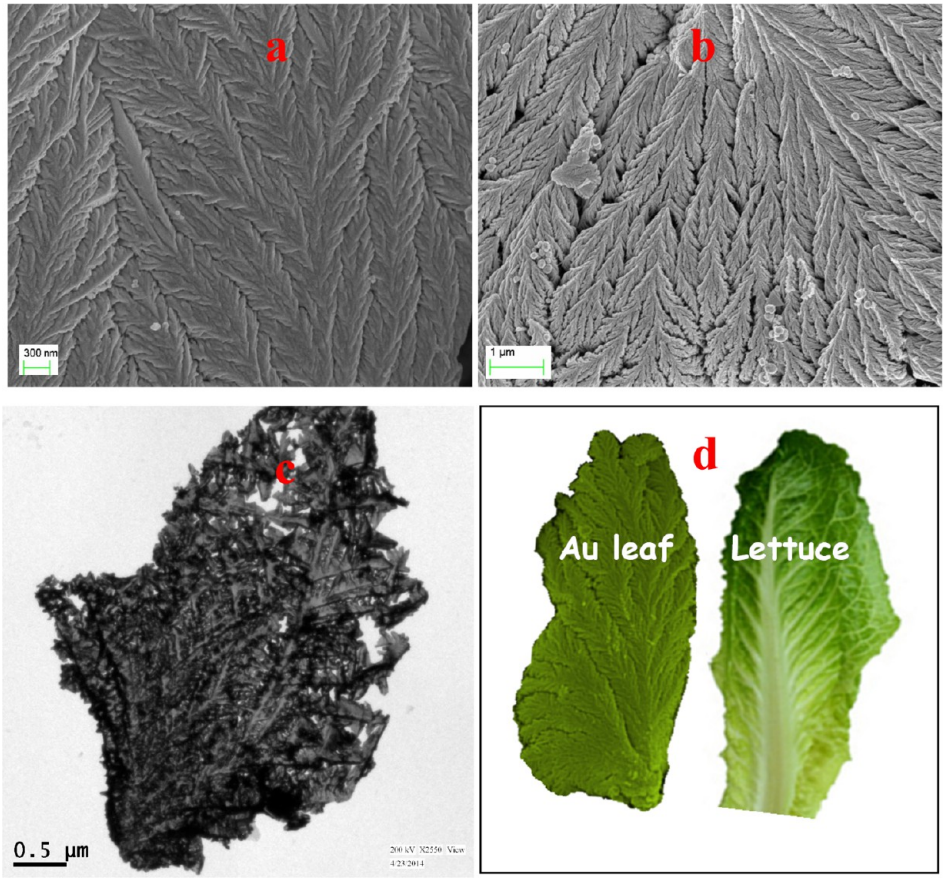

Figure 1. (a, b) FESEM images, (c) TEM image, and (d) comparison with real-time image of MGL.

of chloroauric acid (upper layer) with the dichloromethane solution (lower layer) of 1,4-dihydropyridine ester (DHPE). The reaction is favored through oxidative aromatization of the reducing agent DHPE and subsequent reduction of Au(III) to Au(0). The color change of the upper aqueous layer containing $HAuCl_4$ (yellow to colorless) indicates the completion of the reaction. The as-synthesized product was carefully collected from the liquid−liquid interface and thoroughly washed with ethyl acetate (to remove the excess reducing agent) prior to further characterizations or applications. After the conversion, the organic layer was separated from the biphasic mixture using a micropipet and then solid anhydrous magnesium sulfate was added to the organic layer, and it was kept for 30 min. Then, the organic layer was filtered through cotton wool and the organic solvent DCM was removed by vacuum drying. Finally, the solid product at the bottom of the container was collected for its characterizations. ^{1}H NMR analysis substantiates the facile conversion of DHPE to the corresponding aromatic product during the reduction process of metal ions (Figure S1, Supporting Information). The oxidized aromatic form of DHPE was further confirmed from ESI mass analysis (Figure S2, Supporting Information). HRMS for $C_{13}H_{17}O_4N$ $[M + H]^+$, calculated 252.1236; found 252.1410. DHPE in DCM shows two bands at around 408 and 352 nm in the UV−vis spectra (Figure S3, Supporting Information). Therefore, irradiation at ∼365 nm can easily excite the molecule to act as a reducing agent for Au(III). Two plausible mechanisms (multistep electron transfer[23,24] and direct hydride transfer[23]) are described in Scheme S1 (Supporting Information) for the reduction of $AuCl_4^-$ by DHPE. The yield of the Au nanoleaf synthesis is 98.5%. The above synthetic recipe is also applicable, leading to the successful synthesis of mesoporous leaflike palladium nanostructures (MPL). Thus, the implementation of the "nonaromatic-to-aromatic" electron transfer from DHPE during interfacial reaction becomes very interesting for the fabrication of well-defined noble metal nanostructures, especially palladium, under ambient conditions.

XRD patterns (Figure S4a,c, Supporting Information) of MGL and MPL are in good agreement with the standard JCPDS data (Nos. 040784 and 050681, respectively), and the individual planes are also indicated in the figures. XPS results authenticate the phase purity of the synthesized materials where no other impurity peaks were identified for both MGL and MPL. For MGL, peaks at 83.84 and 87.54 eV in Figure S4b are due to the Au $4f_{7/2}$ and Au $4f_{5/2}$, whereas, for MPL, peaks at 335.23 and 340.48 eV correspond to Pd $3d_{5/2}$ and Pd $3d_{3/2}$ electronic states, respectively (Figure S4d).

FESEM images in Figure 1a,b reveal the leaflike nanostructure of our synthesized MGL, which consist of ultralong primary branches with further subdivision into various secondary branches and so on. The lengths of each secondary and tertiary branch are 1−2 μm and 400−900 nm, respectively. The average width of the smallest branched unit is calculated to be 25−60 nm (Figure S5, Supporting Information). Figure S6 (Supporting Information) depicts the tapping mode AFM image of the as-synthesized MGL, and the thickness of the leaves is calculated to be 25−30 nm. EDAX analysis suggests the large-scale production of uniform gold nanoleaves from our reaction protocol (Figure S7, Supporting Information).

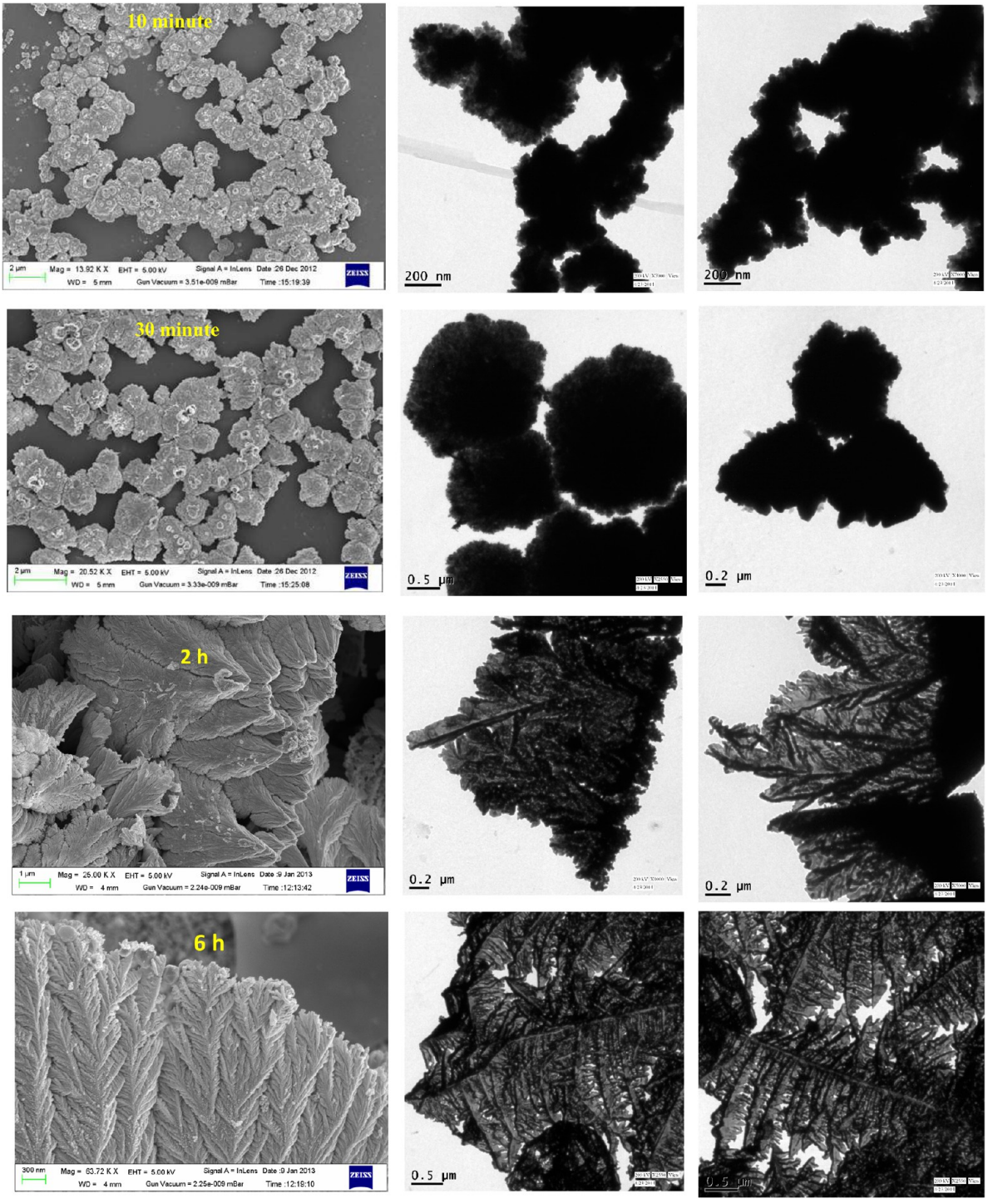

Figure 2. Time-dependent FESEM and TEM images for the growth kinetics of MGL.

The leaflike nanostructure is also evident from the TEM image (Figure 1c), and this unique branched structure is significantly different from the reported dendritic[13−18] or leaflike[19,37] nanostructures; rather, it resembles natural lettuce leaves, as shown in Figure 1d. Here, presumably, the interfacial technique favors the formation of such leaflike superstructures. Assembly of individual units produces a stable layer of gold at the interface, as found in Scheme 1. This leafy nanostructure cannot be fragmented into smaller structures even on strong ultrasonication.

The growth mechanism of the leaflike gold nanostructure was investigated through FESEM and TEM analyses as described in Figure 2. Here, the formation mechanism proceeds through fast nucleation of metallic particles, followed by oriented attachment based on their diffusion-limited growth. The facile redox reaction leads to the initial formation (after 10 min) of irregularly shaped particles of ∼400−500 nm in size that are highly aggregated in nature. Just after the nucleation of metallic particles, incoming ions from the aqueous solution (upper layer) are reduced on the surface of the preformed particles. Outer parts of the structures with a high surface area

dx.doi.org/10.1021/am503251r | ACS Appl. Mater. Interfaces 2014, 6, 9134−9143

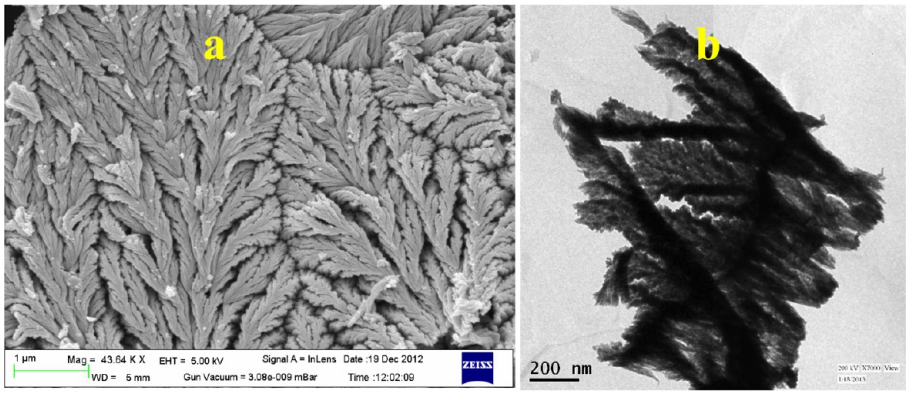

Figure 3. (a) FESEM and (b) TEM images of MPL.

would be the regions in which reorientation and attachment could be more favored than the central parts. As a result, particle size has found to gradual increase with reaction time, which has been confirmed from the TEM images (size of the particles become ~1.5 μm after 30 min). In addition, the outer surfaces of the products after 30 min show some prickly/hierarchical nature, which was absent after 10 min of reaction. Here, it is worth to mention that the darker central region stands as a basic unit from where the leafy/dendritic structures of gold have appeared. After 2 h of reaction time, the products become highly dendritic in nature, although their connection was still present through the basic metallic structures. On prolonged standing of the reaction mixture under UV irradiation, the metallic structures have been fused completely with a large overall flat appearance, and the unique leafy morphology has been identified after 6 h. Here, we kept the reaction medium under UV radiation for 12 h for the sake of completion of the reaction process. The leaflike nanostructures were obtained even in the dark, indicating the prevailing contribution of aromatization reaction over UV irradiation (Figure S8, Supporting Information). Here, the reaction mechanism has been described by the hydride transfer pathway from DHPE to $AuCl_4^-$ (SchemeS2b, Supporting Information). This feature also substantiates that the reduction mechanism is thermodynamically controlled. We have accounted all the reactions under UV light (~365 nm) imposing a faster kinetics to obtain high-quality gold nanoleaves.

The polar organic solvent at the bottom, i.e., DCM or $CHCl_3$, makes DHPE (reductant) soluble, and the upper water layer bears $HAuCl_4$ as oxidant, compelling the aromaticity driven redox reaction (Scheme 1) to take place at the liquid−liquid interface. The density reversal of the solvents, e.g., "water−ethyl acetate" mixture, gives rise to an irregular and divergent broccoli-shaped 3-D morphology, and again, water-miscible organic solvents such as DMSO and CH_3CN are responsible for aggregated spherical structures of gold. Figure S9 (Supporting Information) presents the solvent-dependent morphologies of synthesized gold particles, which clearly imply the advantage of DCM over other used organic solvents for the synthesis of the above-mentioned unique nanostructure of gold.

Addition of other metal halides, such as NaF, NaCl, NaBr, and $NaNO_3$ (having 4 times higher strength than $HAuCl_4$), into the aqueous $HAuCl_4$ layer fails to exhibit any noticeable change in the morphology of synthesized gold nanostructures (Figure S10, Supporting Information), which concludes the supremacy of DHPE as reducing agent for any gold halide solution in the "DCM−water" mixture for the evolution of mesoporous gold leaves. CTAB-modified (10 times higher concentration than $HAuCl_4$) gold chloride aqueous solution takes a longer time (3 days) to complete the reduction due to the micellar barrier at the "DCM−water" interface, and the as-synthesized gold particles (Figure S11, Supporting Information) are found at the bottom of the container, unlike the previous case, as expected from its larger-sized plate-like structures. Here, it is interesting to note that the "DCM−water" interfacial synthetic technique is also highly selective toward DHPE as reducing agent for aqueous $HAuCl_4$ solution for the fabrication of dendritic superstructures under our prescribed reaction conditions. Figure S12 (Supporting Information) shows the FESEM images of Au nanostructures synthesized with various reducing agents and also in the absence of any reducing agents, but these nanostructures are not well-organized as in our DHPE case, which substantiates the superiority of DHPE as not only a reducing agent but also an effective growth controlling agent in our reaction conditions.

The superiority of DCM over other common organic solvents for the fabrication of leafy structure has also been tested for palladium nanostructures. The FESEM image (Figure 3a) suggests a well-organized branched morphology for Pd, and TEM analysis (Figure 3b) also supports the leafy nature of the synthesized Pd nanostructures. Here, the palladium nanoleaves have been synthesized in a very simplified process compared to other reported cases[31,34] for branched palladium nanostructures.

The 3-D leafy structure transpires two different unique surface morphologies: one side of the structure is porous and the other side is nonporous, which is clearly shown in the FESEM image of MGL (Figure 4a and Figure S13a, Supporting Information). In the TEM images (Figure 4b and Figure S13b), the presence of a sharp contrasted area below the dark edges suggests the density variation in the morphology, which preferentially originates from the porous architecture in the synthesized material.[38] Thus, the buoyancy keeps the unique structure in the floating condition. Electron microscopic analyses of Pd also exhibit the similar features that definitely corroborate its porous nature (Figure 4c,d). This porous architecture may originate from its formation mechanism where the liquid−liquid interfacial kinetics tunes the assembly of each individual unit.

At the initial stage, the synthesized nuclei present at the interface bind to the newly formed particles, which can result in the smooth surface of the nanoleaves facing the aqueous side and leaving a porous structure in the organic layer. This porous architecture helps the nanostructure to float over the organic

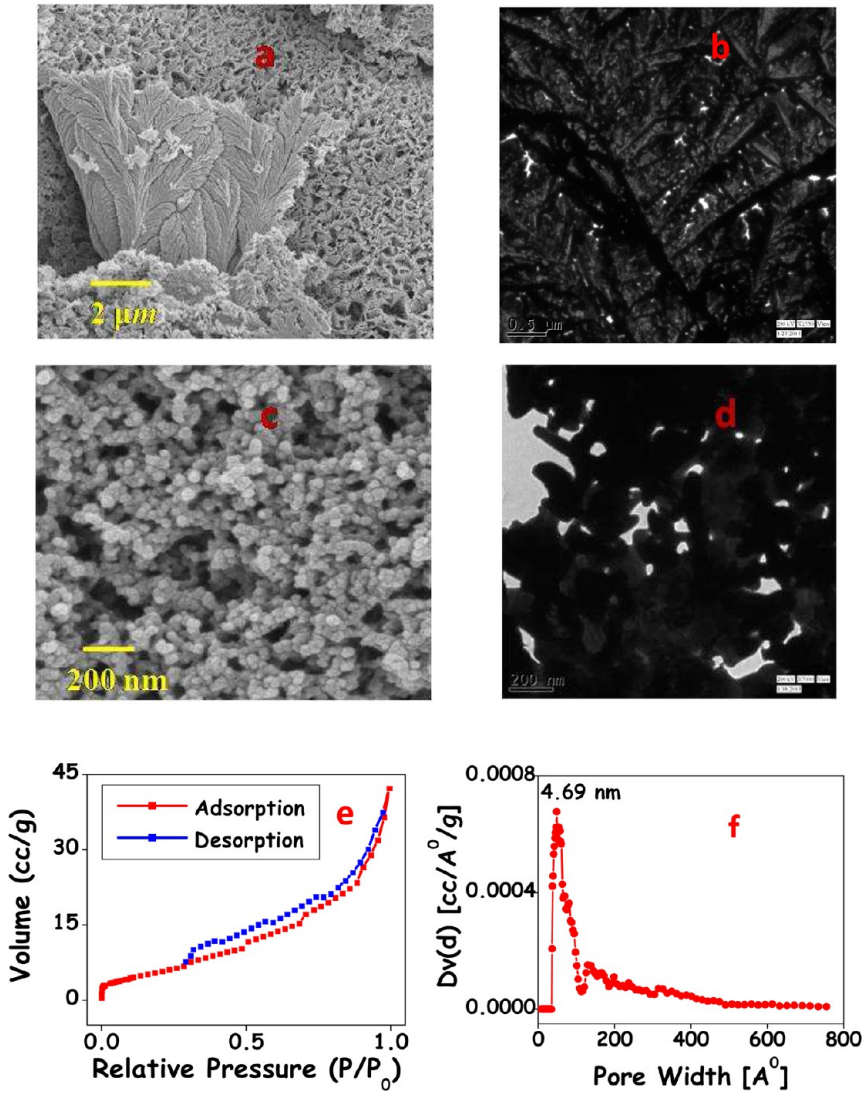

Figure 4. FESEM and TEM images of (a, b) MGL and (c, d) MPL. (e) N_2 adsorption-desorption isotherms and (f) pore-size distribution plot of MPL.

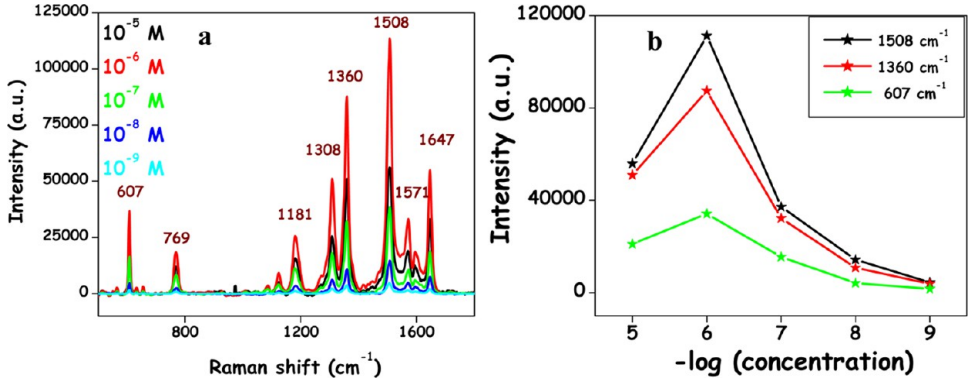

Figure 5. (a) Concentration-dependent SERS spectra. (b) Variation of SERS intensity vs logarithm value of concentration.

layer. A nitrogen adsorption and desorption isotherm experiment was performed to support the porous nature of the as-synthesized materials. Figure S13c shows the N_2 adsorption/desorption isotherm of gold leaves, and the Brunauer–Emmett–Teller (BET) surface area is calculated to be 2.38 $m^2 g^{-1}$. In the case of palladium nanoleaves, the hysteresis loops are shown in Figure 4e, which can be characterized as type IV with a BET surface area of 22.46 $m^2 g^{-1}$. Barrett–Joyner–Halenda (BJH) analysis clearly addresses its mesoporous nature as the average pore size is found to be around 4.7 nm (Figure 4f). The calculated surface areas of MPL or MGL are quite higher than those of some of the reported porous palladium and gold cases, respectively. A comparative table of surface areas is shown in Table S1 (Supporting Information), where, in

dx.doi.org/10.1021/am503251r | ACS Appl. Mater. Interfaces 2014, 6, 9134–9143

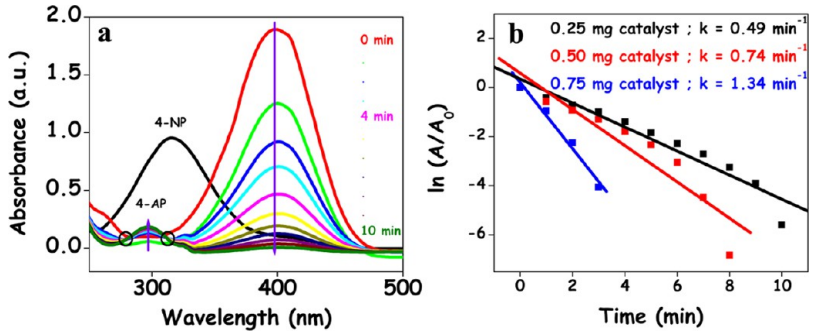

Figure 6. (a) UV−vis absorption spectra of the reduction of 4-nitrophenol by $N_2H_4{\cdot}H_2O$ in the presence of MPL as catalyst. (b) Plot of logarithm of (A/A_0) at 400 nm vs reduction time with varying catalyst amount.

most of the cases, a well-known dealloying process was adopted for the desired structures. Thus, the report presents the mesoporous architecture in the noble metal nanostructures without any roundabout way.

SERS Study. The dendritic superstructures are known to perform exceptionally well as a SERS substrate for their hyperbranched nature, which generates "hot spots" at their edges and corners.[17] Our synthesized leafy gold material enhances the Raman signal of rhodamine 6G (R6G) into a large extent so that we can quantify concentration to the nM level, as described in Figure 5a. The various characteristic Raman peaks of R6G can be assigned as C−C stretching modes for aromatic rings (1647, 1571, 1508, and 1360 cm^{-1}), C−O−C stretching mode (1308 cm^{-1}), C−H in-plane bending (1181 cm^{-1}), C−H out-of-plane bending (769 cm^{-1}), and C−C−C in-plane bending (607 cm^{-1}).[13] Here, all the indicated peaks experienced superior enhancement on MGL compared to normal Raman spectra (NRS) of R6G (Figure S14, Supporting Information), and apparent enhancement factor (AEF) for three peaks (1508, 1360, and 607 cm^{-1}) are calculated to be $\sim 10^7$, as indicated in Table S2 (Supporting Information). The plot of intensity vs log C of the above indicated three peaks suggests that the highest enhancement observed is at 10^{-6} M concentration in each case (Figure 5b), which clearly implies the monolayer formation[39] of R6G on MGL at 10^{-6} M concentration.

Catalysis. In order to evaluate the catalytic activity of our synthesized mesoporous palladium leaves, we have performed the reduction process of 4-nitrophenol (4-NP) as a model catalytic reaction, which can easily be monitored by its visual color change. This reaction has been widely investigated as a model reaction to test the catalytic property of metal nanoparticles by various groups, including ours.[40] The reduced or hydrogenated products of nitroaromatics are aromatic amines, which are the key components in various fields, such as pharmaceuticals, chemical, or dye industries.[41] In most of the cases, sodium borohydride ($NaBH_4$) is used as a potential reducing agent for 4-NP with various catalysts, e.g., noble metal nanoparticles,[42−45] bimetallic,[40,46−48] graphene-noble metal hybrids,[49,50] polymer grafted noble metal nanoparticles,[46] and so on.[51] Although there are some achievements found with hydrazine as reducing agent,[52−54] they are less preferable owing to their drastic reaction conditions (i.e., higher reaction time, elevated temperature) for complete conversion. Recently, Yu et al. reported the hydrogenation of nitroaromatics by hydrazine hydrate in the presence of palladium immobilized carbon nanospheres (Pd/CSs) as a catalyst.[55] In our study, 3 mL of an aqueous solution of 4-NP (10^{-4} M) and hydrazine hydrate (10^{-2} M) were mixed in a quartz cuvette, which results in a deep yellow coloration, and also a red shifting of the corresponding absorbance peak (315 to 400 nm) was found due to the formation of 4-nitrophenolate in alkaline pH.[40] Then, 0.25 mg of MPL was introduced as a catalyst into the reaction mixture, and the absorbance data were collected at an interval of 1 min. The reaction kinetics was monitored by recording the absorbance data of the peak at 400 nm with respect to time and also with the successive evolution of one new peak at around 297 nm due to the formation of 4-aminophenol (4-AP), as shown in Figure 6a. In the absorbance spectra, two isosbestic points are generated, as clearly shown by black circles at around 280 and 313 nm, which confirm 4-AP as a sole product, leaving aside other byproducts.[40] Here, the amount of catalyst and reducing agent is 10 and 100 times higher than the substrate, 4-NP, respectively. In order to authenticate the catalytic property of MPL, various control experiments, such as one blank experiment (without any catalyst), lowering the catalyst's dose (with 0.025 mg of MPL, i.e., same mmol as 4-NP), and lesser hydrazine amount (e.g., 5, 10, and 50 times higher concentrated than used 4-NP), were performed under the same experimental conditions (Figure S15, Supporting Information). The UV−vis spectrum confirms that this is a catalytic process as the absence of catalyst does not show any spectral change, whereas a low catalyst amount (same amount as 4-NP) was sufficient to show the reduction process. The reduction process progresses well even with a lower hydrazine amount, but in a slower rate, which is expected. These results summarize the catalytic property of our synthesized MPL for the reduction of 4-NP by N_2H_4.

Since the added hydrazine (N_2H_4) has a much higher concentration (100 times) compared to 4-NP, the reaction follows the pseudo-first-order reaction kinetics, and the plot of $\ln(A/A_0)$ vs t shows a straight line with a negative slope to point out the rate constant (Figure 6b). The rate constant (k) is calculated to be 0.49 min^{-1} with 0.25 mg of catalyst, and the catalyst activity parameter (ratio of rate constant to amount of catalyst added, i.e., $k_a = k/m$) is found to be 32.67 s^{-1} g^{-1}, which is even higher than the reported cases where $NaBH_4$ has been used as a reducing agent.[49−51] A higher catalyst dose makes the reduction process more facile (Figure S16, Supporting Information), and the rate constant value increases as well (Figure 6b). The present case performed well at room temperature, resulting in complete conversion of 4-NP within a few minutes by $N_2H_4{\cdot}H_2O$ as reducing agent and bare palladium as catalyst, whereas a previous report[55] required 24 h for 83% conversion on refluxing at 80 °C with Pd/CSs as catalyst. MPL also supports the catalytic reduction of other

dx.doi.org/10.1021/am503251r | ACS Appl. Mater. Interfaces 2014, 6, 9134−9143

nitroaromatics, such as 2-nitroaniline and 4-nitroaniline, by hydrazine, again at room temperature, as shown in Figure S17 (Supporting Information).

In order to compare the catalytic efficiency of MPL with Pd NPs, prepared through a reported procedure,[56] we have carried out the catalytic reduction of 4-NP with 0.5 mg of catalyst, but the reduction process is much slower than that of our MPL, as indicated in Figure S18 (Supporting Information). Porous architectures of palladium leafy nanostructures support the "transfer hydrogenation" process quite well for the reduction of nitroaromatics by hydrazine hydrate, which, in turn, converted into nitrogen as byproducts. It is also worthwhile that our synthesized mesoporous gold nanoleaves fail to exhibit catalytic properties under the same reaction environment (Figure S19, Supporting Information), which may be due to their lower BET surface area as well as less catalytic activity for the transfer hydrogenation process compared to our designed mesoporous palladium nanoleaves. The dendritic nanostructure of Pd remained unaltered even after the first catalytic cycle, as found from the FESEM image (Figure S20a, Supporting Information). The BET analysis as described in Figure S20b,c suggests that the average pore size of MPL after the first cycle is ~4.87 nm, which is quite the same to its previous value (4.69 nm) with a lowering in BET surface area (~16.82 m^2/g). MPL stands to be a very effective catalyst for 4-NP reduction by hydrazine at room temperature for three successive cycles, although the rate constant value decreases as expected from the BET analysis (Figure S21, Supporting Information).

Palladium nanostructures catalyzed electrooxidation of formic acid is extremely important due to its low cost and inferior CO poisoning compared to the Pt surface, which encourages us to test the catalytic activities of our synthesized MPL in the formic acid oxidation reaction (FAOR).[57,58] Figure 7 shows the comparative cyclic voltammetric profiles for 0.25 M FA oxidation in the presence of 0.5 M H_2SO_4 by various Pd-based catalysts at a scan rate of 50 mV/s. The CV curve shows two peaks at ~0.3 V in both forward and backward scans, which suggests the direct oxidation of FA to CO_2 with insignificant CO generation as intermediates.[56,58] It is worth mentioning that mass activity (obtained current has been normalized with respect to mass of the catalyst) of MPL is 10 times higher than that of Pd NPs[56] and 6 times higher than that of conventional 20% Pd on carbon.

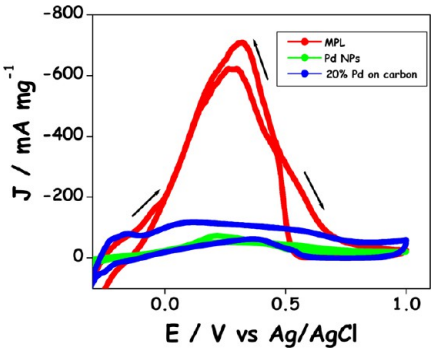

Figure 7. CV curves for formic acid oxidation by various catalysts at 50 mV/s scan rate. {[HCOOH] = 0.25 M; [H_2SO_4] = 0.5 M; and [catalyst] = 14 μg}.

Therefore, our synthesized porous palladium nanostructures are highly effective catalysts in 4-NP reduction by hydrazine at room temperature and also in fuel cell applications.

CONCLUSIONS

In short, a novel synthetic approach has been adopted for the first time to fabricate leaflike nanostructures of both gold and palladium with a porous backbone. The interfacial synthetic technique deals with a 1,4-dihydropyridine derivative in dichloromethane (DCM), which tailors both the morphologies (leaf and porous) of the synthesized noble metals and itself transforms into the aromatic form. Highly branched gold leaves exhibit excellent SERS activity with rhodamine 6G (R6G) as probe molecule. Again, the reduction of nitroaromatics by hydrazine hydrate at room temperature, hitherto an unfamiliar reaction condition, is well-supported by mesoporous palladium as catalyst. The mesoporous palladium also serves as an efficient electrocatalyst for the oxidation of formic acid, leaving a platform for its possible fuel cell applications.

ASSOCIATED CONTENT

Supporting Information

Scheme of the experimental set up; ^{1}H NMR spectra of DHPE and its oxidized product; HRMS of the oxidized aromatic product; UV−vis spectra of DHPE in DCM; proposed reaction mechanisms of the reduction process; XRD pattern and XPS spectra of MGL and MPL; FESEM images, tapping mode AFM images, and EDAX spectra of MGL; FESEM images of gold particles in different experimental conditions; FESEM, TEM images, and BET analysis of porous gold nanoleaves; comparative table of BET surface areas of MGL and MPL with previous reports; NRS spectra of rhodamine 6G with 10^{-3} M ethanolic solution; table of AEF calculation of various Raman bands; UV−visible absorption spectra of reduction process of 4-nitrophenol under various conditions; and reduction process of 4-nitrophenol, 2-nitroaniline, and 4-nitroaniline by hydrazine hydrate in the presence of MPL as catalyst. This material is available free of charge via the Internet at http://pubs.acs.org.

AUTHOR INFORMATION

Corresponding Author

*E-mail: tpal@chem.iitkgp.ernet.in.

Notes

The authors declare no competing financial interest.

ACKNOWLEDGMENTS

The authors are thankful to DST and CSIR, New Delhi, India, for financial assistance, and the IIT Kharagpur for instrumental support. We are also thankful to Prof. Kumar Biradha, IIT Kharagpur, for providing us the facility for the BET surface area measurements.

REFERENCES

(1) Sau, T. K.; Rogach, A. L.; Jackel, F.; Klar, T. A.; Feldmann, J. Properties and Applications of Colloidal Nonspherical Noble Metal Nanoparticles. *Adv. Mater.* **2010**, *22*, 1805−1825.

(2) Liz-Marzan, L. M. Gold Nanoparticle Research Before and after the Brust−Schiffrin Method. *Chem. Commun.* **2013**, *4*, 16−18.

(3) Grzelczak, M.; Perez-Juste, J.; Mulvaney, P.; Liz-Marzan, L. M. Shape Control in Gold Nanoparticle Synthesis. *Chem. Soc. Rev.* **2008**, *37*, 1783−1791.

(4) Sau, T. K.; Murphy, C. J. Seeded High Yield Synthesis of Short Au Nanorods in Aqueous Solution. *Langmuir* **2004**, *20*, 6414−6420.
(5) Sinha, A. K.; Basu, M.; Sarkar, S.; Pradhan, M.; Pal, T. Electrostatic Field Force Directed Gold Nanowires from Anion Exchange Resin. *Langmuir* **2010**, *26*, 17419−17426.
(6) Millstone, J. E.; Park, S.; Shuford, K. L.; Qin, L. D.; Schatz, G. C.; Mirkin, C. A. Observation of a Quadrupole Plasmon Mode for a Colloidal Solution of Gold Nanoprisms. *J. Am. Chem. Soc.* **2005**, *127*, 5312−5313.
(7) Xie, J.; Lee, J. Y.; Wang, D. I. C.; Ting, Y. P. Identification of Active Biomolecules in the High-Yield Synthesis of Single-Crystalline Gold Nanoplates in Algal Solutions. *Small* **2007**, *3*, 672−682.
(8) Wang, Z.; Bharathi, M. S.; Hariharaputran, R.; Xing, H.; Tang, L.; Li, J.; Zhang, Y.-W.; Lu, Y. pH-Dependent Evolution of Five-Star Gold Nanostructures: An Experimental and Computational Study. *ACS Nano* **2013**, *7*, 2258−2265.
(9) Pradhan, M.; Chowdhury, J.; Sarkar, S.; Sinha, A. K.; Pal, T. Hierarchical Gold Flower with Sharp Tips from Controlled Galvanic Replacement Reaction for High Surface Enhanced Raman Scattering Activity. *J. Phys. Chem. C* **2012**, *116*, 24301−24313.
(10) Shin, H.-S.; Hong, J.-Y.; Huh, S. 2-Thiopheneacetic Acid Directed Synthesis of Au Nanorosette as an SERS-Active Substrate. *ACS Appl. Mater. Interfaces* **2013**, *5*, 1429−1435.
(11) Zhang, P.; He, J.; Ma, X.; Gong, J.; Nie, Z. Ultrasound Assisted Interfacial Synthesis of Gold Nanocones. *Chem. Commun.* **2013**, *49*, 987−989.
(12) Sun, Y.; Xia, Y. Shape-Controlled Synthesis of Gold and Silver Nanoparticles. *Science* **2002**, *298*, 2176−2179.
(13) Huang, D.; Qi, Y.; Bai, X.; Shi, L.; Jia, H.; Zhang, D.; Zheng, L. One-Pot Synthesis of Dendritic Gold Nanostructures in Aqueous Solutions of Quaternary Ammonium Cationic Surfactants: Effects of the Head Group and Hydrocarbon Chain Length. *ACS Appl. Mater. Interfaces* **2012**, *4*, 4665−4671.
(14) Qin, Y.; Song, Y.; Sun, N. J.; Zhao, N. N.; Li, M. X.; Qi, L. M. Ionic Liquid-Assisted Growth of Single-Crystalline Dendritic Gold Nanostructures with a Three-Fold Symmetry. *Chem. Mater.* **2008**, *20*, 3965−3972.
(15) Xu, X.; Jia, J.; Yang, X.; Dong, S. A Templateless, Surfactantless, Simple Electrochemical Route to a Dendritic Gold Nanostructure and Its Application to Oxygen Reduction. *Langmuir* **2010**, *26*, 7627−7631.
(16) Ye, W. C.; Yan, J. F.; Ye, Q.; Zhou, F. Template-Free and Direct Electrochemical Deposition of Hierarchical Dendritic Gold Microstructures: Growth and Their Multiple Applications. *J. Phys. Chem. C* **2010**, *114*, 15617−15624.
(17) Jia, W.; Li, J.; Jiang, L. Synthesis of Highly Branched Gold Nanodendrites with a Narrow Size Distribution and Tunable NIR and SERS Using a Multiamine Surfactant. *ACS Appl. Mater. Interfaces* **2013**, *5*, 6886−6892.
(18) Pan, M.; Xing, S.; Sun, T.; Zhou, W.; Sindoro, M.; Teo, H. H.; Yanb, Q.; Chen, H. 3D Dendritic Gold Nanostructures: Seeded Growth of a Multi-Generation Fractal Architecture. *Chem. Commun.* **2010**, *46*, 7112−7114.
(19) Bai, X.; Zheng, L. A Facile Synthesis of Two-Dimensional Dendritic Gold Nanostructures at the Air/Water Interface. *Cryst. Growth Des.* **2010**, *10*, 4701−4705.
(20) Zhu, C.; Peng, H.-C.; Zeng, J.; Liu, J.; Gu, Z.; Xia, Y. Facile Synthesis of Gold Wavy Nanowires and Investigation of Their Growth Mechanism. *J. Am. Chem. Soc.* **2012**, *134*, 20234−20237.
(21) Chen, H.; Wang, Y.; Jiang, H.; Liu, B.; Dong, S. Spontaneous Formation of Two-Dimensional Gold Networks at the Air-Water Interface and Their Application in Surface-Enhanced Raman Scattering (SERS). *Cryst. Growth Des.* **2007**, *7*, 1771−1776.
(22) Lu, G.; Li, C.; Shi, G. Synthesis and Characterization of 3D Dendritic Gold Nanostructures and Their Use as Substrates for Surface-Enhanced Raman Scattering. *Chem. Mater.* **2007**, *19*, 3433−3440.
(23) Zhu, X.-Q.; Liu, Y.-C.; Cheng, J.-P. Which Hydrogen Atom Is First Transferred in the NAD(P)H Model Hantzsch Ester Mediated Reactions via One-Step and Multistep Hydride Transfer? *J. Org. Chem.* **1999**, *64*, 8980−8981.
(24) Jin, M.-Z.; Yang, L.; Wu, L.-M.; Liu, Y.-C.; Liu, Z.-L. Novel Photoinduced Aromatization of Hantzsch 1,4-Dihydropyridines. *Chem. Commun.* **1998**, 2451−2452.
(25) Krishna, K. S.; Sandeep, C. S. S.; Philip, R.; Eswaramoorthy, M. Mixing Does the Magic: A Rapid Synthesis of High Surface Area Noble Metal Nanosponges Showing Broadband Nonlinear Optical Response. *ACS Nano* **2010**, *4*, 2681−2688.
(26) Qin, G. W.; Liu, J.; Balaji, T.; Xu, X.; Matsunaga, H.; Hakuta, Y.; Zuo, L.; Raveendran, P. A Facile and Template-Free Method to Prepare Mesoporous Gold Sponge and Its Pore Size Control. *J. Phys. Chem. C* **2008**, *112*, 10352−10358.
(27) Ding, Y.; Kim, Y.-Z.; Erlebacher, J. Nanoporous Gold Leaf: "Ancient Technology"/Advanced Material. *Adv. Mater.* **2004**, *16*, 1897−1900.
(28) Yan, M.; Jin, T.; Chen, Q.; Ho, H. E.; Fujita, T.; Chen, L.-Y.; Bao, M.; Chen, M.-W.; Asao, N.; Yamamoto, Y. Unsupported Nanoporous Gold Catalyst for Highly Selective Hydrogenation of Quinolines. *Org. Lett.* **2013**, *15*, 1484−1487.
(29) Xu, X.; Li, Y.; Gong, Y.; Zhang, P.; Li, H.; Wang, Y. Synthesis of Palladium Nanoparticles Supported on Mesoporous N-Doped Carbon and Their Catalytic Ability for Biofuel Upgrade. *J. Am. Chem. Soc.* **2012**, *134*, 16987−16990.
(30) Cheong, S.; Watt, J. D.; Tilley, R. D. Shape Control of Platinum and Palladium Nanoparticles for Catalysis. *Nanoscale* **2010**, *2*, 2045−2053.
(31) Watt, J.; Cheong, S.; Toney, M. F.; Ingham, B.; Cookson, J.; Bishop, P. T.; Tilley, R. D. Ultrafast Growth of Highly Branched Palladium Nanostructures for Catalysis. *ACS Nano* **2010**, *4*, 396−402.
(32) Shi, L.; Wang, A.; Zhang, T.; Zhang, B.; Su, D.; Li, H.; Song, Y. One-Step Synthesis of Au-Pd Alloy Nanodendrites and Their Catalytic Activity. *J. Phys. Chem. C* **2013**, *117*, 12526−12536.
(33) Wunder, S.; Polzer, F.; Lu, Y.; Mei, Y.; Ballauff, M. Kinetic Analysis of Catalytic Reduction of 4-Nitrophenol by Metallic Nanoparticles Immobilized in Spherical Polyelectrolyte Brushes. *J. Phys. Chem. C* **2010**, *114*, 8814−8820.
(34) Watt, J.; Young, N.; Haigh, S.; Kirkland, A.; Tilley, R. D. Synthesis and Structural Characterization of Branched Palladium Nanostructures. *Adv. Mater.* **2009**, *21*, 2288−2293.
(35) Zhou, P.; Dai, Z.; Fang, M.; Huang, X.; Bao, J. Novel Dendritic Palladium Nanostructure and Its Application in Biosensing. *J. Phys. Chem. C* **2007**, *111*, 12609−12616.
(36) Eey, S. T.-C.; Lear, M. J. A Bismuth(III)-Catalyzed Friedel−Crafts Cyclization and Stereocontrolled Organocatalytic Approach to (−)-Platensimycin. *Org. Lett.* **2010**, *12*, 5510−5513.
(37) Hong, J.-H.; Hwang, Y.-K.; Hong, J.-Y.; Kim, H.-J.; Kim, S.-J.; Won, Y. S.; Huh, S. Facile Preparation of SERS-active Nanogap-Rich Au Nanoleaves. *Chem. Commun.* **2011**, *47*, 6963−6965.
(38) Sarkar, S.; Pradhan, M.; Sinha, A. K.; Basu, M.; Negishi, Y.; Pal, T. An Aminolytic Approach toward Hierarchical β-Ni(OH)$_2$ Nanoporous Architectures: A Bimodal Forum for Photocatalytic and Surface-Enhanced Raman Scattering Activity. *Inorg. Chem.* **2010**, *49*, 8813−8827.
(39) Dutta, S.; Ray, C.; Sarkar, S.; Pradhan, M.; Negishi, Y.; Pal, T. Silver Nanoparticle Decorated Reduced Graphene Oxide (rGO) Nanosheet: A Platform for SERS Based Low-Level Detection of Uranyl Ion. *ACS Appl. Mater. Interfaces* **2013**, *5*, 8724−8732.
(40) Sarkar, S.; Sinha, A. K.; Pradhan, M.; Basu, M.; Negishi, Y.; Pal, T. Redox Transmetalation of Prickly Nickel Nanowires for Morphology Controlled Hierarchical Synthesis of Nickel/Gold Nanostructures for Enhanced Catalytic Activity and SERS Responsive Functional Material. *J. Phys. Chem. C* **2011**, *115*, 1659−1673.
(41) Mitchell, S. C.; Waring, R. H. *Ullmanns Encyclopedia of Industrial Chemistry*; Wiley-VCH Verlag: Weinheim, Germany, 2000.
(42) Pradhan, N.; Pal, A.; Pal, T. Catalytic Reduction of Aromatic Nitro Compounds by Coinage Metal Nanoparticles. *Langmuir* **2001**, *17*, 1800−1802.

(43) Li, W.; Kuai, L.; Chen, L.; Geng, B. "Re-growth Etching" to Large-sized Porous Gold Nanostructures. *Sci. Rep.* **2013**, *3*, 1−5.
(44) Halder, A.; Patra, S.; Viswanath, B.; Munichandraiah, N.; Ravishankar, N. Porous, Catalytically Active Palladium Nanostructures by Tuning Nanoparticles Interactions in an Organic Medium. *Nanoscale* **2011**, *3*, 725−730.
(45) Fu, G.; Jiang, X.; Ding, L.; Tao, L.; Chen, Y.; Tang, Y.; Zhou, Y.; Wei, S.; Lin, J.; Lu, T. Green Synthesis and Catalytic Properties of Polyallylamine Functionalized Tetrahedral Palladium Nanocrystals. *Appl. Catal., B* **2013**, *138−139*, 167−174.
(46) Pozun, Z. D.; Rodenbusch, S. E.; Keller, E.; Tran, K.; Tang, W.; Stevenson, K. J.; Henkelman, G. A Systematic Investigation of p-Nitrophenol Reduction by Bimetallic Dendrimer Encapsulated Nanoparticles. *J. Phys. Chem. C* **2013**, *117*, 7598−7604.
(47) Zhang, J.; Chen, G.; Guay, D.; Chaker, M.; Ma, D. Highly Active PtAu Alloy Nanoparticle Catalysts for the Reduction of 4-Nitrophenol. *Nanoscale* **2014**, *6*, 2125−2130.
(48) Zhang, P.; Li, R.; Huang, Y.; Chen, Q. A Novel Approach for the in Situ Synthesis of Pt−Pd Nanoalloys Supported on Fe3O4@C Core−Shell Nanoparticles with Enhanced Catalytic Activity for Reduction Reactions. *ACS Appl. Mater. Interfaces* **2014**, *6*, 2671−2678.
(49) Bramhaiah, K.; John, N. S. Hybrid Films of Reduced Graphene Oxide with Noble Metal Nanoparticles Generated at a Liquid/Liquid Interface for Applications in Catalysis. *RSC Adv.* **2013**, *3*, 7765−7773.
(50) Li, J.; Liu, C. Y.; Liu, Y. Au/Graphene Hydrogel: Synthesis, Characterization and Its Use for Catalytic Reduction of 4-nitrophenol. *J. Mater. Chem.* **2012**, *22*, 8426−8430.
(51) Tang, S.; Vongehr, S.; Meng, X. Carbon Spheres with Controllable Silver Nanoparticle Doping. *J. Phys. Chem. C* **2010**, *114*, 977−982.
(52) Luo, P.; Xu, K.; Zhang, R.; Huang, L.; Wang, J.; Xing, W.; Huang, J. Highly Efficient and Selective Reduction of Nitroarenes with Hydrazine over Supported Rhodium Nanoparticles. *Catal. Sci. Technol.* **2012**, *2*, 301−304.
(53) Jagadeesh, R. V.; Wienhofer, G.; Westerhaus, F. A.; Surkus, A.-E.; Pohl, M.-M.; Junge, H.; Junge, K.; Beller, M. Efficient and Highly Selective Iron-Catalyzed Reduction of Nitroarenes. *Chem. Commun.* **2011**, *47*, 10972−10974.
(54) Shi, Q.; Lu, R.; Lu, L.; Fu, X.; Zhao, D. Efficient Reduction of Nitroarenes over Nickel-Iron Mixed Oxide Catalyst Prepared from a Nickel-Iron Hydrotalcite Precursor. *Adv. Synth. Catal.* **2007**, *349*, 1877−1881.
(55) Lu, Y.-M.; Zhu, H.-Z.; Li, W.-G.; Hu, B.; Yu, S.-H. Size-Controllable Palladium Nanoparticles Immobilized on Carbon Nanospheres for Nitroaromatic Hydrogenation. *J. Mater. Chem. A* **2013**, *1*, 3783−3788.
(56) Wang, Q.; Wang, Y.; Guo, P.; Li, Q.; Ding, R.; Wang, B.; Li, H.; Liu, J.; Zhao, X. S. Formic Acid-Assisted Synthesis of Palladium Nanocrystals and Their Electrocatalytic Properties. *Langmuir* **2014**, *30*, 440−446.
(57) Antolini, E. Palladium in Fuel Cell Catalysis. *Energy Environ. Sci.* **2009**, *2*, 915−931.
(58) Wang, Y.; Choi, S.; Zhao, X.; Xie, S.; Peng, H.-C.; Chi, M.; Huang, C. Z.; Xia, Y. Polyol Synthesis of Ultrathin Pd Nanowires via Attachment-Based Growth and Their Enhanced Activity towards Formic Acid Oxidation. *Adv. Funct. Mater.* **2014**, *24*, 131−139.